ELSEVIER

Contents lists available at ScienceDirect

Applied Surface Science

journal homepage: www.elsevier.com/locate/apsusc



Full Length Article

Temperature-adaptive MoN-Ag coatings under operando tribology: multiscale Ag diffusion-oxidation coupling

Yong Cheng ¹, Yupeng Zhang ¹, Yiqun Feng ⁰, Meiqi Zhang, Aiying Wang ^{*}, Zhenyu Wang ^{*}

State Key Laboratory of Advanced Marine Materials, Zhejiang Key Laboratory of Extreme-environmental Material Surfaces and Interfaces, Ningbo Institute of Materials Technology and Engineering, Chinese Academy of Sciences, Ningbo 315201, China

ARTICLE INFO

Keywords:
Temperature-adaptive
HiPIMS
MoN-Ag coatings
Operando friction
Transfer film

ABSTRACT

The development of temperature-adaptive lubricant coatings for foil air bearings remains a major challenge. Here, dense MoN–Ag nanocomposite coatings with varying Ag contents (0–22.8 at.%) were deposited by HiPIMS–DCMS. The coatings exhibited low residual stress, strong adhesion, and high mechanical performance. Tribological tests showed that the coefficient of friction (COF) decreased with Ag addition at 350 °C and 500 °C, reaching 0.389 and 0.223, respectively, for the 22.8 at.% Ag coating. At 600 °C, however, the COF increased with Ag content, while the 13.4 at.% Ag coating displayed the lowest wear rate of 2.84 \times 10 5 mm 3 N 1 m $^{-1}$. Under simulated service conditions, the 13.4 at.% Ag coating demonstrated a reduction in COF from \sim 0.4 to 0.26 across 25–600 °C, evidencing self-adaptive lubrication. This behavior is ascribed to the formation of a low-shear-strength surface layer, where Ag diffusion and the generation of MoO $_{\rm x}$, Ag $_{\rm 2}$ MoO $_{\rm 4}$, and Ag $_{\rm 2}$ MoO and Ag

1. Introduction

Air foil bearings operate by floating on a cushion of air or inert gas, which minimizes wear and friction due to the absence of direct physical contact between components. This design offers low resistance, broad applicability, high energy efficiency, and reduced emissions [1], making it suitable for high-temperature and high-speed applications. Including air circulation compressors, micro-generators, cryogenic turbo-compressors, turbochargers and turbomachinery [2,3]. However, during start-up and shutdown phases, direct contact between the shaft and foil occurs sliding friction, significantly affecting bearing longevity and reliability. The application of solid lubricant coatings on the shaft and foil surfaces via advanced surface coating technologies can effectively alleviate these issues.

Transition metal nitride (TMN) coatings are known for their high mechanical strength, excellent chemical stability, and superior wear resistance, leading to their widespread use in cutting tools, molds, automotive components, and mechanical bearing protection. Among them, MoN coatings exhibit self-lubricating characteristics attributed to the formation of Magnéli-phase MoO₃. This phase features easy-sliding

surfaces along the (101) crystal plane, which reduces friction and enables prolonged operation under severe conditions [4–6]. However, MoO_3 has strong volatility above 500 °C, severely limiting high-temperature durability of MoN coatings [7].

In recent years, the strategic integration of multiple lubricating phases and the formation of self-generated lubricating phases on coating surfaces have emerged as key approaches for achieving low friction coefficients over a wide temperature range. TMN, known for their high hardness and thermal stability, have been widely investigated in this context. Zhang et al. [8] developed a self-lubricating VAIN/Ag coating by optimizing the Ag content, achieving low COF from room temperature (RT) up to 600 °C. Similarly, in CrAlYN coatings, the formation of Cr₂O₃ has been directly linked to effective lubrication in friction tests conducted at both RT and 700 °C [9]. To further extend the temperature range of low friction, multicomponent coating designs have been explored, capitalizing on the synergistic effects of different elements. For instance, Wu et al. [10] systematically studied the tribological behavior of MoN(Ag-W) composite coatings and found that multiple oxides, including MoO3 and Ag2MoO4 formed during friction, contributing to excellent high-temperature performance.

E-mail addresses: aywang@nimte.ac.cn (A. Wang), wangzy@nimte.ac.cn (Z. Wang).

^{*} Corresponding author.

¹ These authors contributed equally to this work.

In Ag-containing nitride coating systems, the adaptive lubricating behavior is governed by two key interrelated mechanisms: the thermally driven diffusion of Ag and the kinetics of surface oxidation. At relatively low temperatures (typically below 400 °C), Ag atoms rapidly diffuse along structural defects such as columnar grain boundaries toward the wear track. This process results in the formation of a soft metallic lubricating layer that effectively lowers the COF [11,12]. As the temperature rises to the medium-high range (400-700 °C), the coating's oxidation resistance becomes critical. In systems such as MoN-Ag, however, oxidation is not a failure mechanism but instead contributes to adaptive lubrication. Studies have shown that layered ternary oxides, such as Ag₂MoO₄ and Ag₂Mo₄O₁₃, formed from reactions between Ag and elements like Mo or V, exhibit intrinsically favorable lubricating properties [8,13,14]. The overall oxidation kinetics, governed by the interplay of oxide nucleation, growth, and Ag diffusion rates, ultimately determine the coating's durability and stability under high-temperature service conditions.

Although previous studies have demonstrated the excellent widetemperature-range performance of MoN-Ag coatings [15,16], few have explored the use of high-power impulse magnetron sputtering (HiPIMS) for deposition. Moreover, Most investigations focus on friction behavior under constant temperatures, neglecting the operando friction behavior across varying temperatures.

Physical vapor deposition (PVD) has become a key technique for fabricating MoN-based coatings due to its low processing temperatures, broad substrate compatibility, precise deposition control, and environmental friendliness [17]. HiPIMS is an advanced magnetron sputtering technology that combines direct-current magnetron sputtering (DCMS) with pulsed power supply, offering superior controllability during deposition [18]. This method significantly enhances coating adhesion, mechanical properties, wear resistance, and corrosion resistance. For instance, Ying et al. [19] fabricated dense WS2 coatings via HiPIMS and compared them with RF-sputtered WS2, which exhibited a loose, porous structure. In contrast, the HIPIMS-deposited coatings suppressed columnar growth, resulting in a denser, more uniform, and smoother surface. These structural differences led to markedly improved mechanical properties: the HiPIMS-deposited sample had a hardness of 4.76 GPa, far exceeding the 0.21 GPa of the RF-sputtered coating. The HiPIMS coating also showed higher H/E and H³/E² ratios and better adhesion, indicating superior wear resistance. Similarly, Alhafian [20] compared TiAlN coatings deposited by HiPIMS and cathodic arc evaporation (CAE). While both coatings had similar hardness, the HiPIMSprepared TiAlN exhibited a lower elastic modulus, higher H/E and H³/E² values, a 30 % reduction in COF, and a lower wear rate (WR), confirming its enhanced tribological performance.

In this study, MoN-Ag nanocomposite coatings with different Ag contents were fabricated using a HiPIMS-DCMS system. The mechanical properties, microstructure, and tribological behavior of the coatings were systematically evaluated over a wide temperature range. To simulate realistic operating conditions, an operando friction test was designed to elucidate tribological evolution from 25 to 600 °C. TEM and micro-area XRD confirmed that the diffusion and aggregation of Ag on the coating surface, together with the formation of $\rm MoO_x$ and $\rm Ag-Mo-O$ compounds (AgTM_xO_y) contributed to enhanced lubricating performance.

2. Experiment

2.1. Coating deposition

MoN-Ag coatings with different Ag contents were deposited on silicon wafers, high-speed steel, and nickel-based superalloy substrates using a self-assembled hybrid HiPIMS-DCMS system. Prior to deposition, all substrates were ultrasonically cleaned in acetone and ethanol for 15 min. The cleaned substrates were then mounted on the sample holder using conductive adhesive and transferred into the vacuum chamber.

Once the vacuum level reached 3.0×10^{-5} Pa, the substrate surface was etched for 30 min using a linear anode layer ion source to remove surface oxides and contaminants. The etching process was performed under an Ar flow rate of 45 mL/min (working pressure: 0.20 Pa), with an ion source current of 0.2 A, a voltage of 1200 V, and a substrate bias of -200 V. After etching, a Mo transition layer was first deposited using a HiPIMS-powered Mo target operated at an average power of 1500 W, a duty cycle of 5 %, a pulse width of 50 µs, a frequency of 1000 Hz, and a substrate bias of -200 V for 15 min. To improve adhesion, a MoN interlayer was subsequently deposited for 10 min. Finally, the MoN-Ag coatings were deposited under a substrate bias of -150 V, with Ar and N2 flow rates set at 50 mL/min and 60 mL/min, respectively (working pressure: 0.41 Pa). The Ag content was controlled by varying the DC power applied to the Ag target: 0 W, 50 W, 100 W, and 200 W, corresponding to samples labeled S1, S2, S3, and S4. The Mo target was powered by a HiPIMS supply operating at an average power of 1700 W, a duty cycle of 2.5 %, a pulse width of 50 µs, and a frequency of 500 Hz. The deposition time was extended by 30 min for each stepwise increase in Ag target power to ensure a consistent coating thickness across all samples. The equipment schematic is shown in Fig. 1.

2.2. Microstructural characterizations

The phase composition of the coatings deposited on high-speed steel was characterized by X-ray diffraction (XRD, Bruker AXS D8 Advance, Germany) using Cu Ko radiation with scanning angle ranging from 20 to 80°. Residual stress was measured on coatings deposited on silicon wafers using a SuPro FST5000 thin-film stress meter, which applies the substrate curvature method and Stoney's equation to evaluate film stress. Cross-sectional morphology of the coatings on silicon wafers was examined by field emission scanning electron microscope (Verios G4 UC). Surface morphology and elemental composition, as well as worn surfaces after tribological tests on nickel-based superalloy substrates, were observed using a Quanta 250 FEG SEM equipped with an energydispersive X-ray spectrometer (EDS) operating at an accelerating voltage of 15 kV. Mechanical properties were characterized using a Nano Indenter G200 system with a Berkovich diamond indenter (apex angle 70.32°, tip radius 30 nm). Hardness (H) and elastic modulus (E) were determined by the continuous stiffness measurement (CSM) method, with the indentation depth limited to one-tenth of the coating thickness to minimize substrate effects. The tests were conducted at a loading strain rate of 0.05 s⁻¹ and an unloading rate of 4 mN/s. Adhesion strength was assessed by scratch testing on high-speed steel substrates using a CSM Revetest instrument equipped with a Rockwell diamond cone indenter (120° apex angle, 200 μm tip radius). The load was linearly increased from 0 to 150 N over a scratch length of 5 mm at a speed of 1.5 mm/min. Each coating was tested at least three times to ensure reproducibility. The critical load (Lc3) corresponding to coating delamination and substrate exposure was identified using SEM observation of the scratch tracks. Phase transformations after friction tests were investigated using a VANTEC500 micro-area XRD system with a two-dimensional detector (spot size 0.5 mm²) and a Renishaw confocal Raman spectrometer with a 532 nm laser source. Raman spectra were acquired from three separate locations to ensure reliability. The chemical bonds of the coatings were analyzed using X-ray photoelectron spectroscopy (XPS, Axis Ultra DLD) performed on a Kratos spectrometer, which utilized monochromatic Al K α radiation (photon energy, $h\nu$ 1486.7 eV) as the X-ray source. Transmission electron microscopy (TEM) was carried out using a Talos F200X electron microscope operating at 200 kV. TEM specimens were prepared via focused ion beam (FIB) milling (Carl Zeiss, Auriga).

2.3. Tribological tests

The tribological properties of the coatings deposited on nickel-based superalloy substrates were evaluated using a high-temperature ball-on-

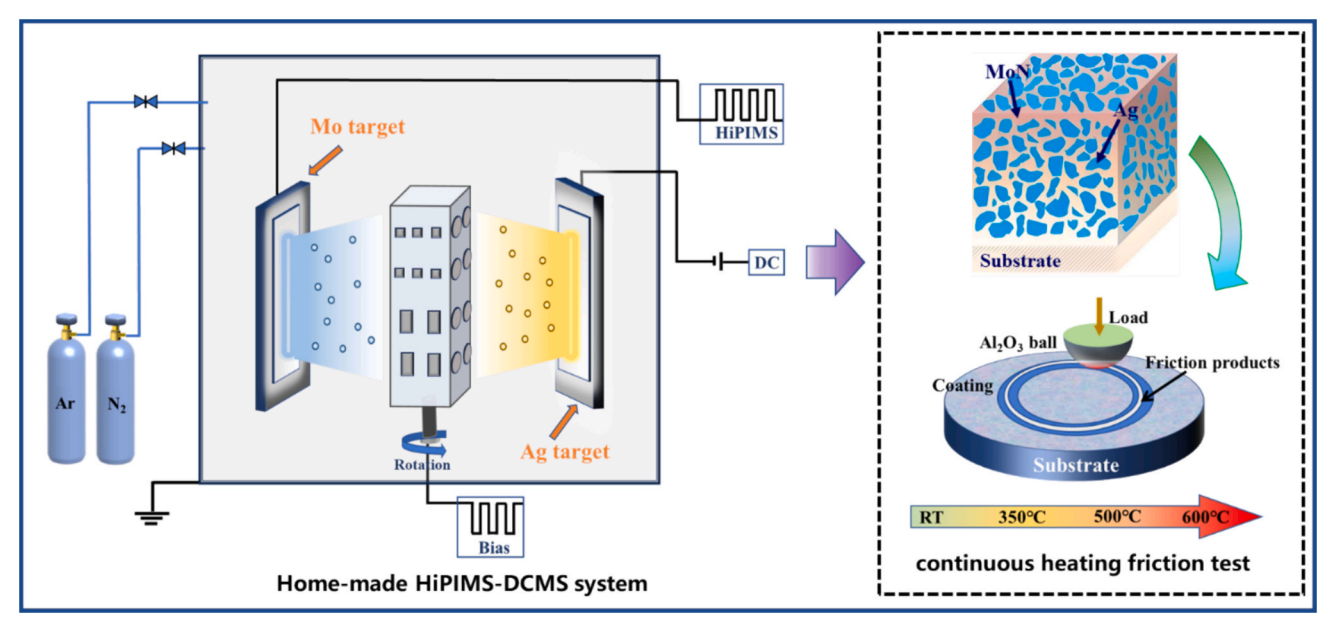


Fig. 1. Schematic diagram of the equipment and continuous heating friction test.

disk tribometer (Anton Paar, THT). Tests were conducted at RT, 350 °C, 500 °C, and 600 °C. To simulate real service conditions, an operando friction test was designed using a stepwise heating protocol: the same sample was tested successively at 25 °C, 350 °C, 500 °C, and 600 °C, with the temperature raised to the next level immediately after completing the previous test stage. Both isothermal tests (separate samples at each temperature) and the operando test (continuous heating on one sample) were performed for comparison. The test configuration included a $\phi 6$ mm Al_2O_3 ball as the countermovement component, with a rotational speed of 5 cm/s, an applied load of 2 N (resulting in Hertzian contact pressures between 982.6 to 1129.8 MPa), a wear track radius of 5 mm, and sliding distances of 100 m.

The WR was determined using the following formula [21]:

$$W_R = \frac{S \times l}{N \times L} \tag{1}$$

where S represents the cross-sectional area of the abrasion mark (mm²); *l* denotes the track length (mm); N is the applied load (N); L is the total sliding distance (m).

3. Results

3.1. Microstructural and composition analyses

By varying the Ag target power, four MoN-Ag coatings with silver contents of 0 at.%, 8.8 at.%, 13.4 at.%, and 22.8 at.% were successfully deposited, designated as S1 to S4. As shown in Fig. 2, all coatings exhibit uniform and compact surface morphology without visible cracks or voids, which can be attributed to the utilization of highly ionized HiPIMS technology. With increasing Ag content, the coating surfaces become more particulate and porous, mainly due to the agglomeration and diffusion of Ag atoms during deposition [22]. Cross-sectional images reveal that all coatings possess a well-defined multilayered structure, consisting of a Mo transition layer, a Mo₂N interlayer, and a MoN-Ag top layer. The total thickness controlled between 4.5 and 5.0 μ m. A sharp interface between the coating and the substrate indicates strong adhesion, while the microstructure shows typical columnar growth characteristics.

The phase composition of MoN-Ag coatings with different Ag contents is shown in Fig. 3(a). The S1 coating (without Ag) consists of a face-

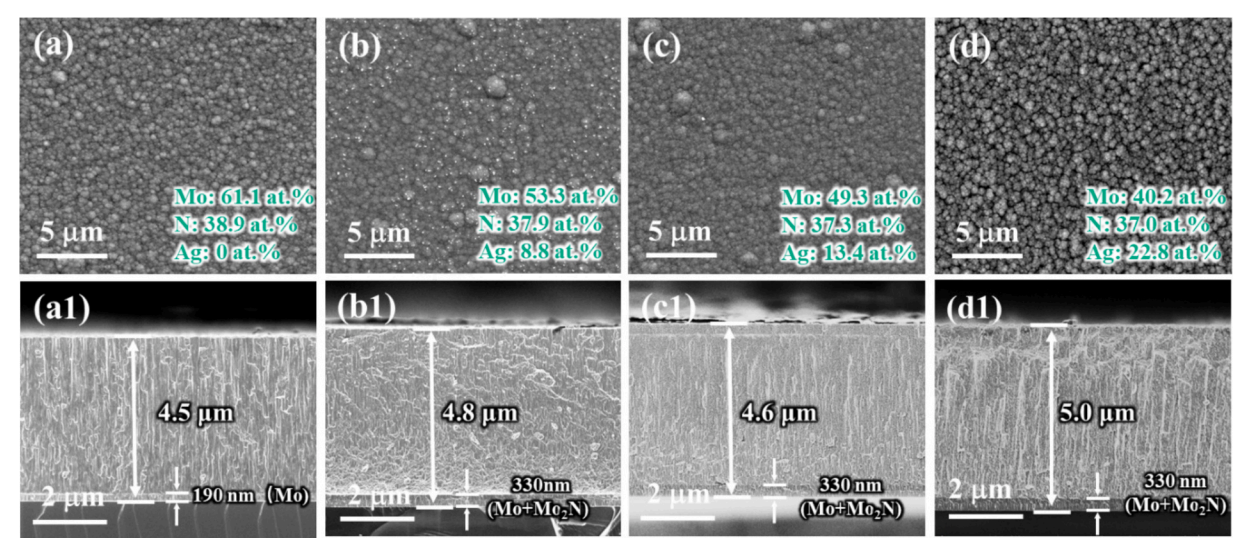


Fig. 2. Surface and cross-sectional morphologies of different coatings, (a, a1) S1; (b, b1) S2; (c, c1) S3; (d, d1) S4.

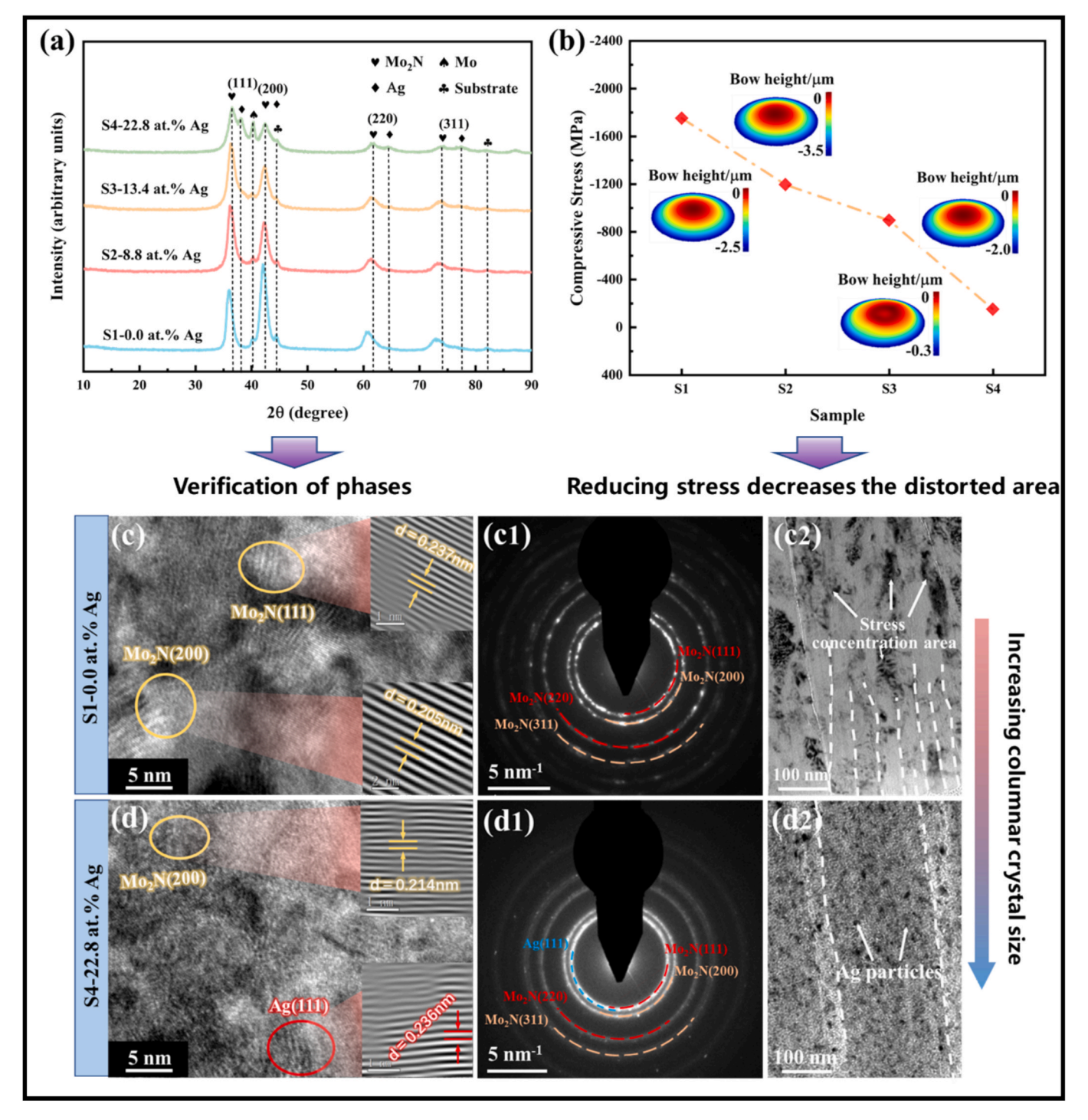


Fig. 3. (a) XRD; (b) The calculated residual stress of all deposited coatings; The microstructure of (c), (c1), c2): S1 and (d), (d1), (d2): S4 coatings characterized by STEM, SAED and HRTEM mode.

centered cubic Mo_2N phase (ICDD 25–1366) and a metallic Mo phase (ICDD 42–1120), with a preferred orientation along the Mo_2N (200) plane. The observed Mo diffraction peaks are likely attributable to the Mo transition layer. With the incorporation of Ag, coatings S2-S4 clearly display diffraction peaks corresponding to cubic Mo_2N , Mo, and metallic Ag (ICDD 04–0783), confirming the successful integration of Ag into the coatings. Notably, the preferred orientation shifts from Mo_2N (200) to Mo_2N (111) as Ag is added.

An important benefit of Ag doping is the reduction of residual stresses in the coatings. The macroscopic average residual stress (σ_f) of S1-S4 coatings was calculated using the Stoney formula, as expressed in

Equation (2) [23]:

$$\sigma_{film} = \frac{1}{6} * \frac{E_s h_s^2}{(1 - \nu_s)^* h_c} * \left(\frac{1}{R_s} - \frac{1}{R_c}\right)$$
 (2)

where E_S and ν_s represent the elastic modulus (GPa) and Poisson's ratio of the substrate material, respectively; h_s denotes the substrate thickness (m), h_c stands for the coating thickness (Å); R_s is the radius of curvature of the coating (Å), and R_c is the radius of curvature of the substrate (Å).

The calculated residual stress values (Fig. 3(b)) indicate a notable decrease from -1752 MPa to -149 MPa with increasing Ag content.

This reduction is primarily attributed to the capacity of soft Ag particles to absorb strain energy as the composite coating deforms elastically or plastically under external loading [24].

As shown in Fig. 3(c2), the width of columnar crystals in the undoped MoN coating exhibit widths range from 30 to 50 nm, with clearly visible distorted regions and blurred boundaries due to stress concentration. Fig. 3(d2) reveals that with Ag incorporation, the columnar crystal size increases to 150-200 nm. And the distorted regions disappear, which can be attributed to the reduction in residual stress induced by Ag addition. HRTEM analysis of the S1 coating (Fig. 3(c)) shows lattice spacings of 0.237 nm and 0.205 nm, corresponding to the Mo₂N (111) and (200) planes, respectively. These findings are consistent with the polycrystalline diffraction rings of Mo₂N in the SAED pattern (Fig. 3 (c1)). The absence of Mo diffraction rings confirms that the Mo peaks observed in the XRD pattern originate from the transition layer. For the S4 coating (Fig. 3(d)), HRTEM images reveal lattice spacings of 0.207 nm and 0.205 nm, assigned to the Mo₂N (200) and Ag (111) planes, respectively. The corresponding SAED pattern (Fig. 3(d1)) shows an additional diffraction ring associated with Ag. Due to the similar lattice parameters of Ag and Mo₂N, their diffraction rings overlap considerably.

3.2. Mechanical properties

Fig. 4(a) illustrates the gradual decrease in hardness and elastic modulus of the MoN-Ag coatings with increasing Ag content. The S1 coating (without Ag) exhibited the highest values, with H and E reaching 24.1 GPa and 343.9 GPa, respectively. While the S4 coating recorded the lowest values of 9.7 GPa and 219.9 GPa. This softening trend is attributed to the intrinsic softness of metallic Ag, which, due to its low shear strength, promotes interfacial sliding when present in significant proportions within the coating. A concomitant reduction in residual compressive stress also contributes to the decrease in hardness.

The ratios H³/E² and H/E are widely recognized as key indicators of

coating toughness and wear resistance. Specifically, $\mathrm{H}^3/\mathrm{E}^2$ reflects the resistance to plastic deformation, while H/E is positively correlated with fracture toughness. Higher values generally indicate better mechanical performance, reduced plastic deformation, lower wear rate, and improved ability to withstand strain without failure [25]. As depicted in Fig. 4(b), both H/E and $\mathrm{H}^3/\mathrm{E}^2$ decrease with rising Ag content, suggesting a reduction in overall toughness and wear resistance. Load-displacement curves of the MoN-Ag coatings are presented in Fig. 4(c). All samples display smooth curves without discontinuities, indicating a low density of internal defects and a relatively dense, uniform coating structure. Coatings with lower Ag content require higher loads to reach the same indentation depth, further confirming that Ag incorporation reduces the coating's resistance to penetration, consistent with the decline in hardness.

The adhesion strength between the coating and substrate is a critical factor determining coating durability, which defines continuous and widespread delamination exposes a significant portion substrate under critical load. As shown in Fig. 4(d), all coatings exhibit excellent adhesion strength, with critical loads (Lc3) exceeding 105 N. The adhesion strength initially decreases but then increases with Ag content, reaching a maximum value of 122 N for the coating with 22.8 at.% Ag (S4). The reduction in adhesion from S1 to S2 can be attributed to the decreased hardness and toughness of the coating, which impair its load-bearing capacity. An inverse correlation exists between compressive stress and adhesion strength: lower residual stresses improve adhesion [26]. High compressive stresses can induce peeling, wrinkling, or crack formation, thereby compromising interfacial integrity. As indicated in Fig. 3(b), the incorporation of Ag effectively reduces compressive stress in the coatings, which contributes to the improved adhesion strength observed from S2 to S4.

MoN-Ag coatings with similar phase structures and comparable Ag contents were selected for comparison, as summarized in Table 1. The results indicate that the hardness of MoN-Ag coatings generally

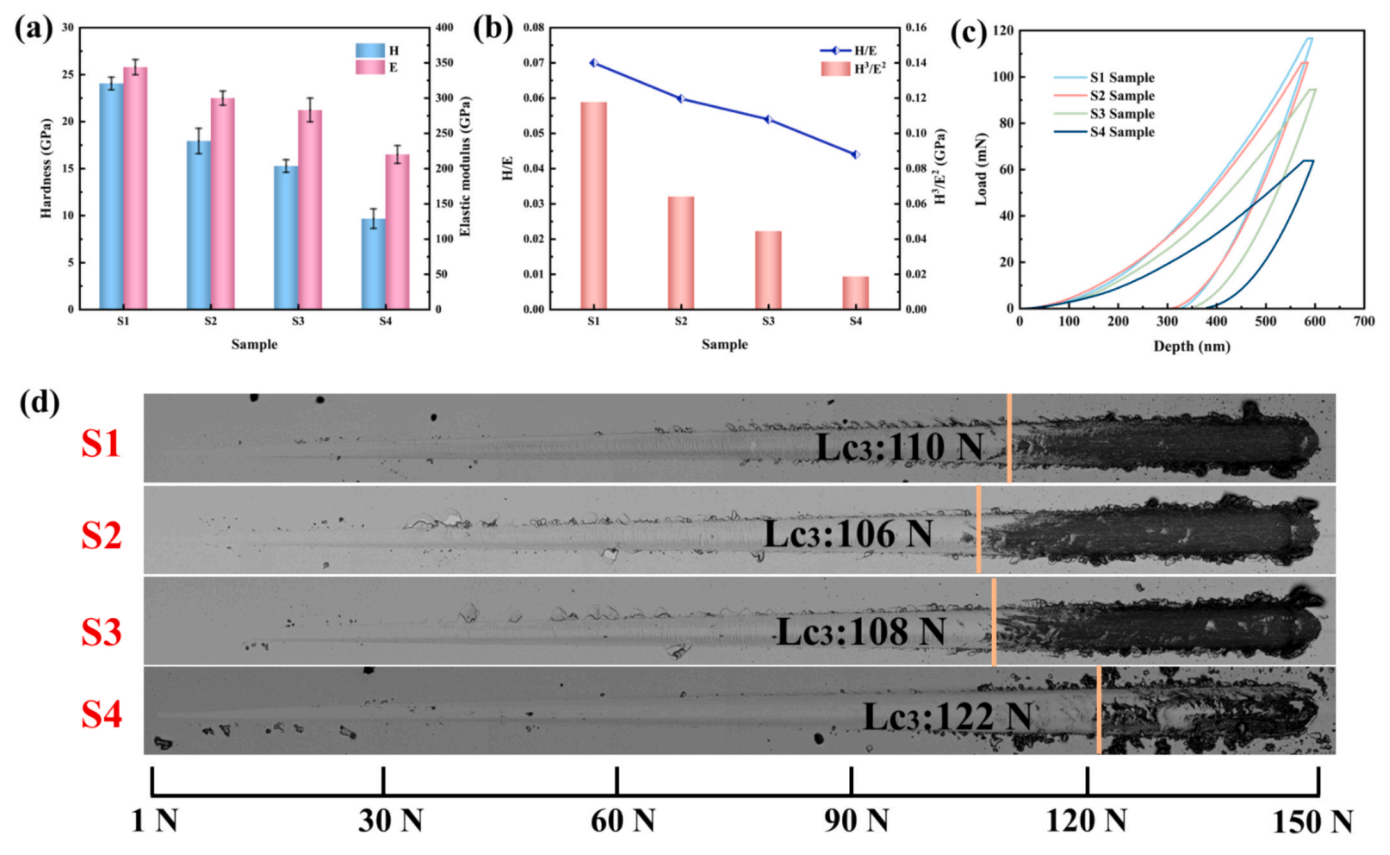


Fig. 4. (a) H and E; (b) H³/E² and H/E (c) Load-displacement curves (d) SEM images of the scratch test of all MoN-Ag coatings.

Table 1
Hardness and Elastic modulus values of similar coatings developed by other researchers.

Ag Content (at.%)	Deposition method	Hardness (GPa)	Elastic modulus (GPa)	References
0/8.8/13.4/ 22.8	HiPIMS-DCMS	24.1/17.9/ 15.3/9.7	343.9/299.8/ 283.1/219.9	Our work
0/12.1/ 26.9	Radio Frequency	17.6/20.5/ 16.2	281.4/310.5/ 292.4	[27]
0/12.5/ 15.3	Magnetron sputtering	24/10.8/8.3	_	[28]
0/11.6	DCMS	26/15.1	_	[16]
0/6.2/26.1	HiPIMS	26/13.9	_	[29]
0	Radio Frequency	18	284.4	[30]
0/7.9/17.3	DCMS	12.9/8.1/4.5	220.5/163.3/ 100.0	[15]

decreases with increasing Ag content. Notably, under equivalent Ag content conditions, the coatings developed in this study demonstrate higher hardness than those reported in previous works. This enhancement can be attributed to the use of advanced HiPIMS coating technology. Study employing HiPIMS technology [28] has also demonstrated superior mechanical properties.

3.3. Constant temperature friction

Fig. 5(a) presents the average COF of the S1-S4 coatings at RT, with values of 0.389, 0.456, 0.462, and 0.473, respectively. These results indicate that the incorporation of Ag does not significantly reduce the COF at RT. At 350 °C, however, the S4 coating exhibited the lowest COF, stabilizing around 0.389, and a clear decreasing trend in COF was observed with increasing Ag content across all coatings. While nitride coatings typically show high COF at low to medium temperatures, Ag doping is shown here to moderately lower the COF within this range. At 500 °C, the COF of all coatings decreased significantly, with average values of 0.388, 0.352, 0.324, and 0.223 for S1 to S4. At 600 °C, the S1 coating failed completely due to the formation of volatile MoO3, and thus its COF and WR could not be measured. Under the same condition, the S2, S3, and S4 coatings exhibited average COF values of 0.274, 0.293, and 0.306, respectively. Overall, these findings demonstrate that Ag-doped MoN-Ag composite coatings effectively reduce the COF at low and medium temperatures, and significantly improve friction performance at high temperatures, thereby extending the service temperature range of MoN-based coatings.

Fig. 5(b) illustrates the WR of the coatings at different temperatures. The lowest WR occurred at RT, while the highest was observed at 600 $^{\circ}$ C, indicating that wear intensified with increasing temperature. After tests at RT, 350 $^{\circ}$ C, and 500 $^{\circ}$ C, the S1 coating exhibited the lowest WR, whereas S4 showed the highest. In contrast, after the 600 $^{\circ}$ C test, S2 (lower Ag) displayed the highest WR, while S3 (intermediate Ag) demonstrated the lowest, suggesting an optimal Ag content for high-temperature wear resistance.

3.4. Continuous heating friction behavior

Based on its superior performance in the constant temperature tests, the S3 coating was selected for the operando friction evaluation. Fig. 6 (a) exhibit consistent COF values at each temperature stage. At RT, the COF initially increased, followed by a slight drop before stabilizing around 0.4. When the temperature reached 350 °C, interaction between the coating and counterpart ball within the original wear track induced fluctuations in COF that gradually increased to approximately 0.36. At 500 °C, the COF stabilized quickly after a short running-in period, decreasing to about 0.32. During the 600 °C stage, the COF remained stable after run-in, maintaining a value around 0.26. As illustrated in Fig. 6(b), the lowest WR was 5.4×10^{-6} mm³N⁻¹m⁻¹ at RT. WR progressively increased with temperature, indicating material depletion within the wear track and increased wear severity. The COF and WR indicate that lubricating material remained in the wear track after three friction stages, preserving high-temperature lubrication properties at 600 °C.

4. Discussion

4.1. Phase transformation

To further elucidate the tribological mechanisms, micro-area XRD and Raman spectroscopy were performed on the wear tracks after friction tests at various temperature ranges. As shown in Fig. 7(a), no significant phase changes were observed after testing at RT and RT-350 °C, with only Mo₂N, Ag, and minor MoO₃ detected. At the RT-350 °C stage, intensified Ag diffraction peaks indicate substantial diffusion toward the coating surface. When the temperature reached 500 °C, the thermal diffusion rate increased significantly, allowing Ag to migrate more readily along the columnar grain boundaries of the MoN-Ag coating and form a low-shear-strength lubricating film [15]. Concurrently, intensified tribochemical reactions led to the formation of layered Ag₂MoO₄ and Ag₂Mo₄O₁₃ phases with weak interlayer shear strength. During

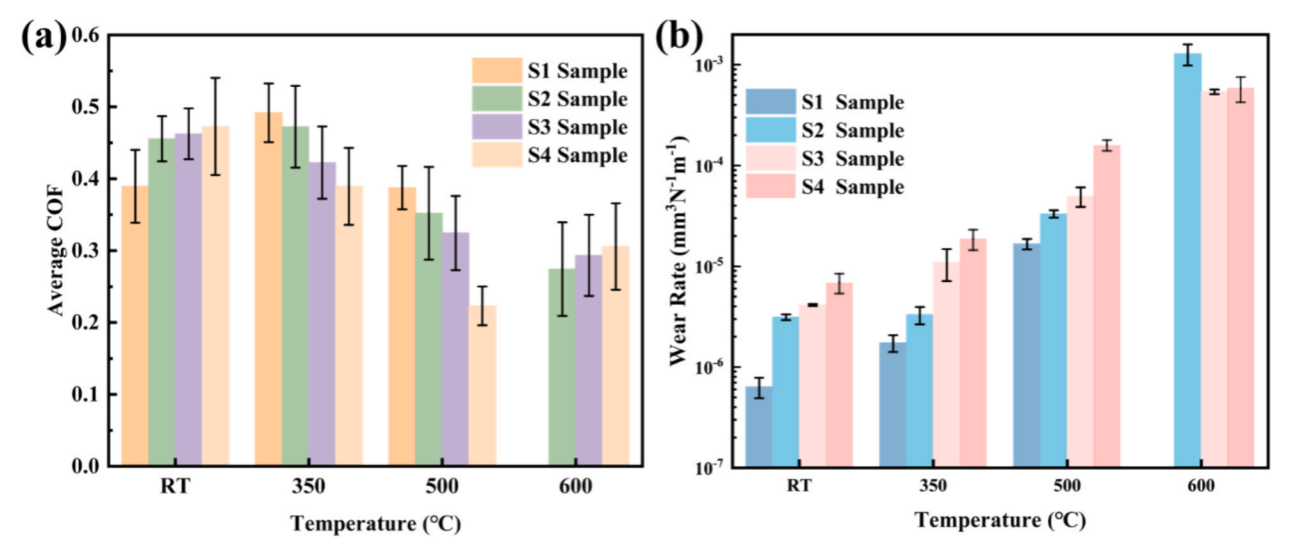


Fig. 5. Average friction coefficient (a), and wear rate (b) of S1-S4 coatings at 25 °C, 350 °C, 500 °C, 600 °C.

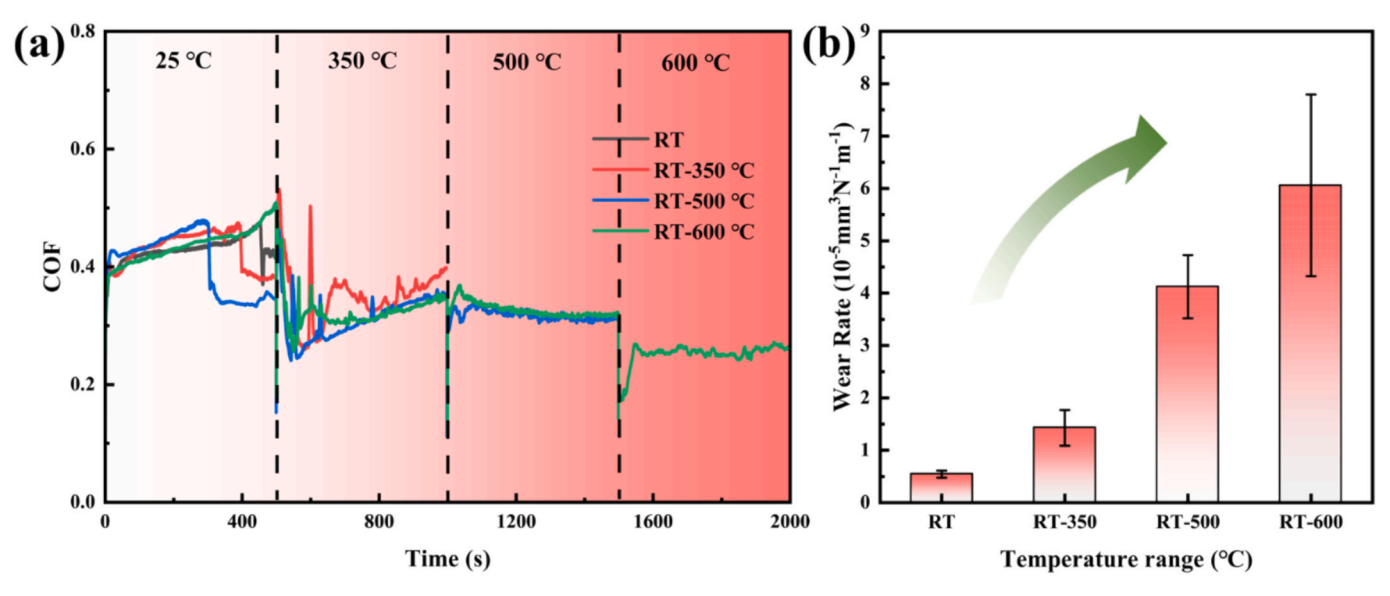


Fig. 6. The friction curves (a) and corresponding WR (b) during continuous heating friction of S3 sample.

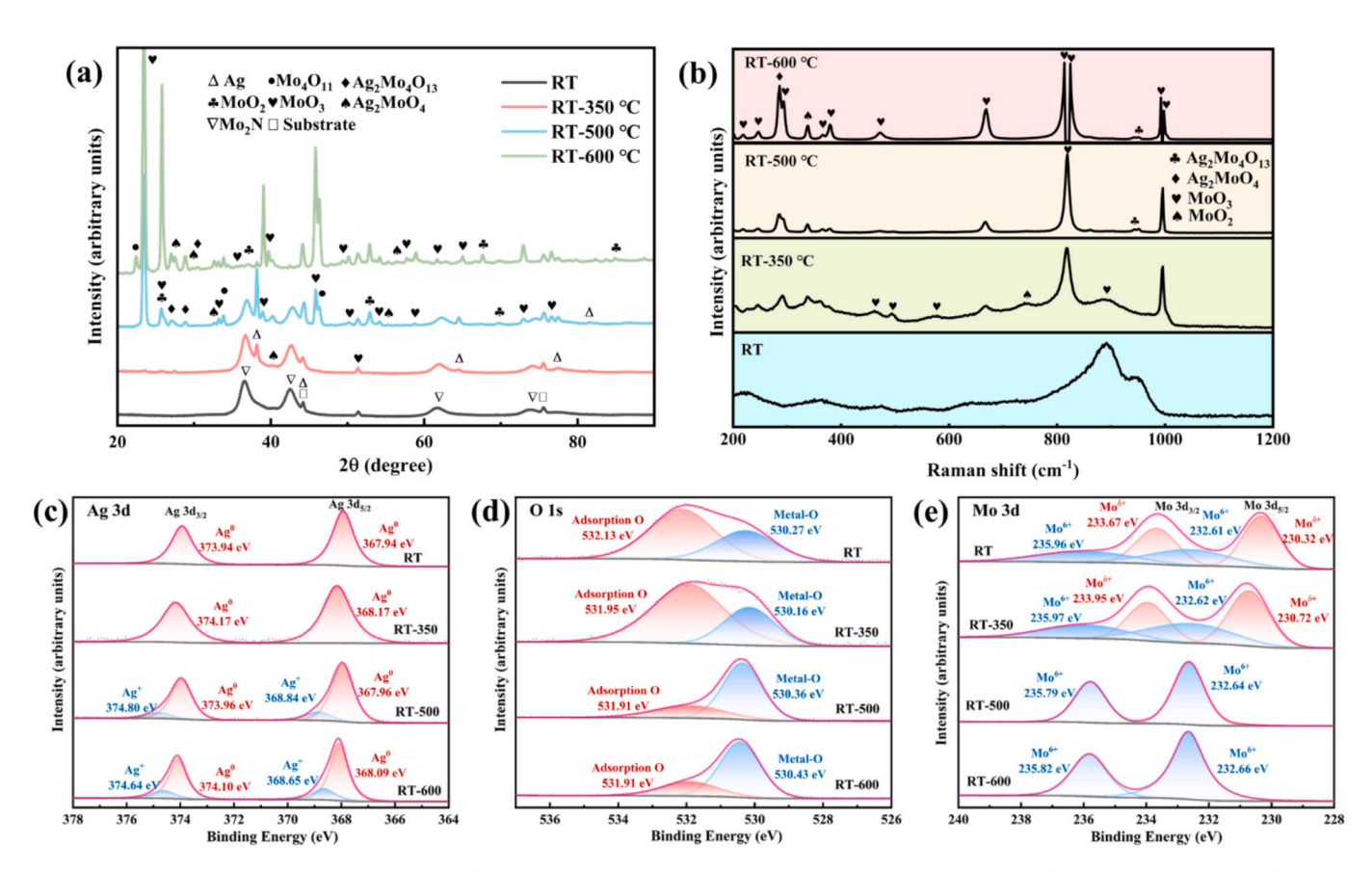


Fig. 7. The micro-area XRD pattern (a); Raman (b) and the fitted XPS spectra of S3 sample: (c)Ag 3d (d) O 1 s (e)Mo 3d at the wear track after operando friction.

high-temperature friction, the molecular bonds between layers in bimetallic oxide lubricating phases synergistic Ag-oxides and Magnéliphase MoO_3 are easily broken and interlayer slipping, resulting in excellent lubrication properties [31–33].

To corroborate the formation of lubricating phases, Raman spectroscopy was used to analyze the phase composition within the wear tracks. As shown in Fig. 7(b), MoO $_3$ was detected in the wear tracks after tests at RT and RT-350 °C. Weaker peaks corresponding to $Ag_2Mo_4O_{13}$ and MoO_2 were also observed, suggesting that under the combined

action of friction and heating, Ag_2MoO_4 and MoO_2 can form in the wear track, albeit in amounts too low to be detected by XRD.

Based on XPS analysis of the surface chemical states of MoN-Ag coatings after friction at different temperatures, combined with XRD and Raman results, the evolution of lubricating phases is systematically illustrated Fig. 7(c-e). For the RT and RT-350 °C samples, the Mo 3d spectrum shows doublet peaks at 230.32 eV and 233.67 eV, corresponding to $\mathrm{Mo}^{\delta+}$ (0 $<\delta<3$) in Mo₂N [34], along with a weak Mo⁶⁺ signal near 232.61 eV, indicating trace amounts of MoO₃ [35]. This

finding is corroborated by the MoO₃ vibrational peak detected in the Raman spectroscopy. The Ag 3d peaks appear at 367.94 eV $(3d_5/2)$ and 373.94 eV $(3d_3/2)$, confirming the presence of metallic Ag on the worn surface [36]. The significantly enhanced Ag signal in the RT-350 °C sample indicates that elevated temperature promotes Ag diffusion along columnar grain boundaries. The O 1 s spectrum shows a characteristic peak at 530.27 eV attributed to Mo-O bonds, and a broad peak at 532.13 eV associated with adsorbed oxygen and surface hydroxyl groups, reflecting localized oxidation during friction. At 500 °C, the intensity of the Mo⁶⁺ peak in the Mo 3d spectrum increases markedly, with binding energies shifting to 232.64 eV (3d₅/₂) and 235.79 eV $(3d_3/_2)$, corresponding to Mo-O coordination in $Ag_2Mo_4O_{13}$ and Ag₂MoO₄. Simultaneously, a new peak appears in the Ag 3d spectrum at $368.74\,$ eV, assigned to ${\rm Ag}^+,$ confirming the formation of ternary Ag-Mo-O oxides. At 600 °C, the Mo⁶⁺ peak shifts toward higher binding energies, and the proportion of Ag⁺ further increases, indicating enhanced Ag oxidation and restructuring of Mo-O bonds at higher temperatures. The reduced peak area at 531.91 eV in the O 1 s spectrum suggests a higher degree of crystalline oxide formation, consistent with the stronger oxide-related diffraction peaks in XRD. Overall, the XPS analysis reveals the dynamic evolution of surface chemistry, where frictioninduced Mo-O bond reorganization and Ag oxidation lead to the formation of a multicomponent lubrication system comprising layered Ag-

Mo-O oxides, metallic Ag, and Magnéli-phase MoO_x.

The reaction equation of lubricating phases from RT to 600 $^{\circ}$ C based on the XRD and Raman results are as follows [37,38]:

$$Mo + 3/2O_2 \rightarrow MoO_3 \tag{3}$$

$$2Ag + Mo + 2O_2 \rightarrow Ag_2MoO_4 \tag{4}$$

$$2Ag + 4MoO_3 + 1/2O_2 \rightarrow Ag_2Mo_4O_{13}$$
 (5)

4.2. Analysis of the wear track and counterpart ball morphology

Fig. 8(a, b) shows that during the first and second temperature stages, minimal material was transferred to the surface of the counterpart ball, indicating a predominantly dry friction with limited adhesion. The surface topography of the counterpart ball after the third stage (Fig. 8(c)), reveals a greater amount of transferred material on the contact surface, which is attributed to increased adhesion at elevated temperatures. Nevertheless, the contact surface remained smooth, with no visible ploughing grooves and only minimal wear, suggesting that easy shear of the coating material helped to maintain coating integrity and reduce the COF. When the temperature reached 600 °C, the wear track became saturated with a liquid-like lubricant phase, and significant amounts of lubricating material were transferred to the contact

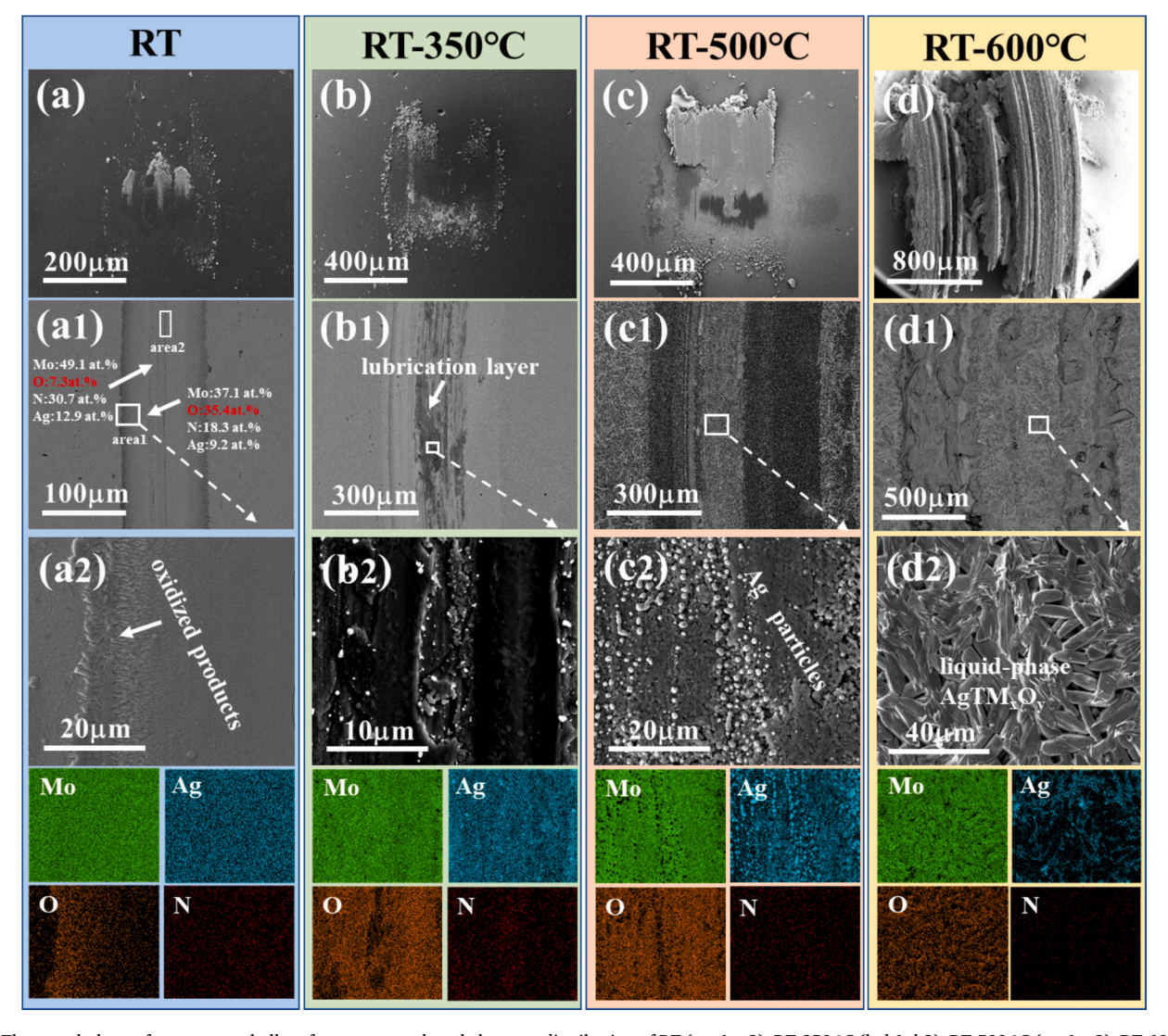


Fig. 8. The morphology of counterpart ball surface, wear track and elements distribution of RT (a, a1, a2); RT-350 °C (b, b1, b2); RT-500 °C (c, c1, c2); RT-600 °C (d, d1, d2) after continuous heating friction of S3 sample.

surface of counterpart ball due to the adhesion effect.

Fig. 8(a1) showes the morphology of the wear track after the first stage (RT). The friction-induced layer accumulated mainly in the non-load-bearing regions along both sides of the track. EDS spot analysis indicated an oxygen content of 7.3 at.% in the central load-bearing area, compared to 35.4 at.% at the track edges. This finding indicates that oxidized products generated during friction were progressively pushed toward the edges, leaving the central region under dry friction conditions. The absence of an effective lubrication layer in this region contributed to a higher COF. A magnified view (Fig. 8(a2)) shows oxides being extruded to the track periphery and compacted into a lamellar structure by the counterpart ball. Elemental mapping confirms that this oxide layer consists of a homogeneous mixture of Mo and Ag oxides.

After the second stage (Fig. 8(b1, b2)), the oxide distribution extended into the load-bearing region. Enlarged views and elemental maps confirm that the tribolayer was composed of Mo and Ag oxides, with Ag particles contributing to improved lubrication. By the third stage (Fig. 8(c2)), Ag particles had aggregated into larger clusters within the tribolayer. Structurally, the columnar grain morphology of the coating provides intercolumnar gaps that facilitate the transport of Ag particles to the surface [39]. As the columnar grain size increases, these gaps widen, promoting more extensive Ag diffusion. The pressure difference at the particle interface can be found according to Gibbs-Thomson equation (6) [40] which is:

$$\Delta p = p_{in} - p_{out} = \gamma \left(\frac{1}{R_1} + \frac{1}{R_2}\right) \tag{6}$$

where Δp is the pressure difference between the interfaces, γ is the surface free energy, and R_1 and R_2 are the radii of curvature of the inner and outer surfaces of Ag particles

According to the Gibbs-Thomson effect, the chemical potential of Ag particles varies with particle size, as expressed in equation (7):

$$\Delta \mu = \Delta p V_m = \frac{2\gamma V_m}{r} \tag{7}$$

where $\Delta\mu$ represents the change in chemical potential, r is the radius of spherical Ag particles, and V_m is the molar volume of Ag atoms.

According to equation (7), a smaller Ag particle radius (r) corresponds to a larger $\Delta\mu$, indicating a higher detachment rate of Ag atoms from the particles [41]. Consequently, Ag particles with a larger radius exhibit a lower percentage of atom separation. As temperature increases, Ostwald ripening enhances atomic detachment and migration, leading to the coalescence of smaller Ag particles into larger aggregates [42]. Grain boundary defects facilitate the growth of Ag particles; however, as the particles enlarge, the limited space within these defects restricts further expansion inside the MoN-Ag coating [43]. When the temperature or holding time increases, the driving force for Ag growth exceeds the spatial constraints of the defects, resulting in Ag diffusion and aggregation on the coating surface. At 350 °C, Ag accumulates as fine particles on the surface, while at 500 °C, accelerated diffusion promotes the formation of larger Ag clusters. This explains both the aggregation of silver on the worn surface and the larger size of Ag particles observed in the third stage compared to the second stage.

Outside the Ag-rich regions, the tribolayer shows co-localization of Mo, Ag, and O elements. Combined with the results presented in Fig. 7, these observations confirm that the tribolayer in these areas contains lubricating oxide phases such as $Ag_2Mo_4O_{13}$, Ag_2MoO_4 , and MoO_3 . The presence of these oxides, together with soft silver particles, contributes to a significant reduction in the COF.

Fig. 8(d1) show the morphology of the wear track after the fourth stage. The central part of the track, which serves as the main load-bearing area, experiences the most severe wear, resulting in a thinner lubrication layer in the middle and a thicker layer near the edges. A magnified view in Fig. 8(d2) reveals that the tribolayer contains relatively large rectangular particles embedded in a lubricating phase that

exhibits characteristics of plastic flow. Elemental mapping analysis, along with the findings from Fig. 7, confirms that the rectangular particles are Mo oxides, while the plastic flow region consists of Ag-O bioxide lubricating compositions. According to previous studies [44], silver molybdate compounds (Ag₂MoO₄ and Ag₂Mo₄O₁₃) have a low melting point (about 574 °C and 563 °C, respectively). As a result, they undergo a solid–liquid phase transition, forming a liquid-phase lubrication film on the sliding surface. This lubrication mechanism effectively reduces friction, explaining the coating exhibits the lowest COF observed at 600 °C [45].

4.3. Analysis of microstructure

The internal microstructure of the wear track on the S3 coating after the friction at RT-500 °C was characterized by TEM. As shown in Fig. 9 (a), high-temperature friction induced significant microstructural evolution, resulting a two-layer structure: a dense MoN-Ag nanocomposite coating at the bottom and an oxide-rich tribolayer on the top. Agglomerated particles were observed within the tribolayer, and selected-area electron diffraction (SAED) of Area 1 confirmed that these particles consist of face-centered cubic Ag, which is consistent with SEM observations. EDS analysis further revealed that the oxide tribolayer contains O-rich phases incorporating Mo and Ag.

The SAED pattern taken from Area 3 showed diffraction rings corresponding to Mo₂N and Ag phases, confirming that the coating beneath the tribolayer remains structurally intact and unoxidized. Fig. 9(b) presents an HRTEM image of the coating interior, where lattice spacings of 0.204 nm and 0.235 nm were identified in larger particles as belonging to the Ag phase, while the surrounding region with a lattice spacing of 0.241 nm was attributed to the Mo₂N phase. These results demonstrate that Ag nanoparticles within the coating aggregated to form Ag-enriched particles at Mo₂N grain boundaries as temperature increased. According to the Ostwald ripening principle, as temperature rises and holding time extends, Ag particles accumulated within the coating migrate toward the surface, forming larger Ag particles. SAED in area2 and the HRTEM image in Fig. 9(c) show lattice spacings of 0.198 nm, 0.231 nm, 0.249 nm, and 0.343 nm, corresponding to the MoO₃ phase, while lattice spacings of 0.204 nm, 0.241 nm, 0.325 nm, and 0.33 nm were assigned to Ag, MoO2, Ag2MoO4, and Ag2Mo4O13 phases. These findings indicate that the tribolayer predominantly consists of Mo oxides, Ag-Mo bi-oxides, and Ag particles.

4.4. Discussion of lubrication mechanism

To illustrate the operando friction mechanism of the MoN-Ag nanocomposite coatings, a schematic diagram is shown in Fig. 10. As shown in Fig. 10(a), a small amount of MoO_x and $AgTM_xO_y$ forms within the wear track at RT. However, due to the limited quantity of these compounds, most are extruded out of the wear track during friction, preventing the formation of a continuous lubrication film in the loadbearing area. As a result, only minimal material transfers to the counterpart ball surface, and no continuous transfer film is established. Dry friction between the counterpart ball and the coating contributes to the highest COF. At 350 °C, Ag atoms migrate toward the coating surface and aggregate into metallic Ag particles. The combined lubricating action of these soft Ag particles and the formed MoO_x and Ag-Mo-O oxides within the tribolayer leads to a noticeable reduction in the COF. At 500 °C, accelerated Ag diffusion promotes the formation of larger Ag clusters on the surface, further enhancing lubrication. The increased temperature enhances adhesion, expanding the transfer material area. A smooth and continuous transfer film forms on the counterpart ball surface, which protects the coating and contributes to a lower COF. At $600\,^{\circ}$ C, severe Mo oxidation results in the formation of large rectangular particles protruding from the coating surface. After contacting the coating on the counterpart ball, the rectangular MoO_x particles are first compacted and contacted with the generated AgTM_xO_v in the wear track

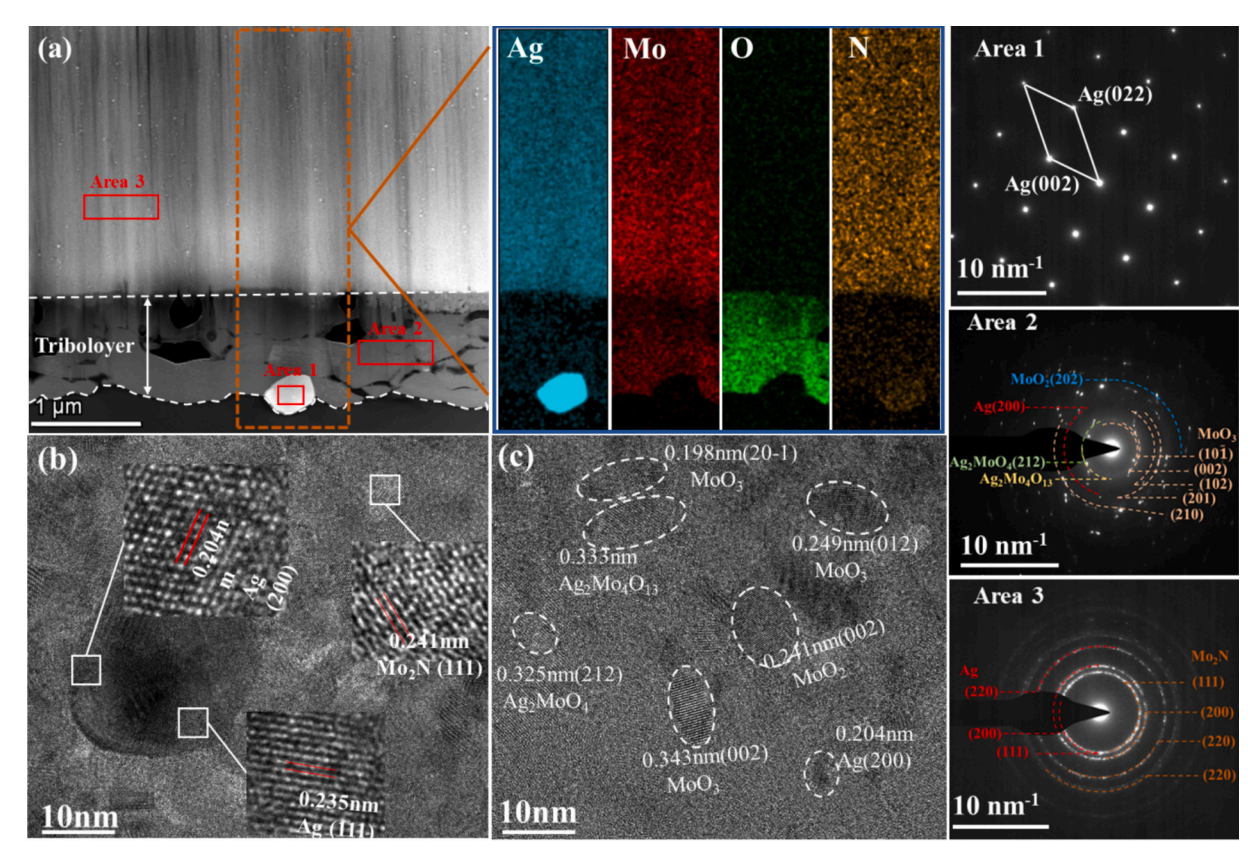


Fig. 9. Microstructure of S3 coating after continuous heating friction test at RT-500 °C.

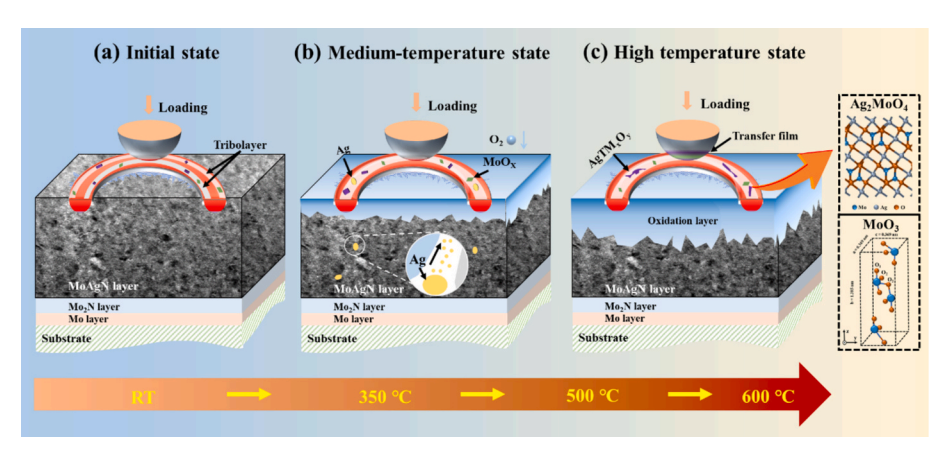


Fig. 10. The element diffusion and tribology mechanism of S3 coating over RT-600 °C.

after continued friction, forming a morphology of MoO_x particles arranged in phase with $AgTM_xO_y$. Due to the adhesion effect, a significant amount of lubricant material is transferred to the contact surface of counterpart ball. The sliding interface is effectively lubricated by a liquid-like Ag-Mo-O oxide film (formed due to the low melting point of silver molybdates), resulting in the lowest COF observed.

5. Conclusions

In this study, MoN-Ag coatings with Ag content varying from 0 to 22.8 at. % were successfully fabricated using a HiPIMS-DCMS system. The effect of Ag on the microstructure and tribological properties of coatings were discussed. In particular, the tribological performance was evaluated both under fixed temperatures and operando conditions from 25 $\,^{\circ}\text{C}$ to 600 $\,^{\circ}\text{C}$. This work provides a reliable framework for

understanding the lubrication behavior of MoN-Ag coatings under realistic high-temperature service conditions. The main conclusions are as follows:

- (1) The dense microstructure strengthening results in high mechanical properties (24.1 GPa) and strong adhesion (122 N) of MoNAg coatings. Meanwhile, the Ag incorporation reduced residual compressive stress from -1752 MPa to -149 MPa.
- (2) The coating with 13.4 at.% Ag exhibited self-adaptive lubrication behavior over RT-600 $^{\circ}$ C, along with the lowest WR, attributed to microstructural evolution and the formation of a low-shear-strength tribolayer.
- (3) The tribology mechanism was revealed in terms of the diffused Ag synergistic the formation of MoO_x , Ag_2MoO_4 , $Ag_2Mo_4O_{13}$

lubricating phases with layered structure, which slipping along the crystal plane that contributes to the reduction of COF.

CRediT authorship contribution statement

Yong Cheng: Writing – original draft, Visualization, Validation, Methodology, Data curation, Conceptualization. Yupeng Zhang: Writing – review & editing, Validation, Methodology, Investigation, Data curation. Yiqun Feng: Writing – review & editing, Formal analysis, Data curation. Meiqi Zhang: Writing – review & editing, Methodology, Data curation. Aiying Wang: Writing – review & editing, Supervision, Resources, Project administration, Methodology, Investigation, Funding acquisition, Data curation. Zhenyu Wang: Writing – review & editing, Supervision, Resources, Project administration, Methodology, Investigation.

Declaration of competing interest

The authors declare that they have no known competing financial interests or personal relationships that could have appeared to influence the work reported in this paper.

Acknowledgments

The work was financially supported by the National Key R&D Program of China (2024YFB3816500), the National Natural Science Foundation of China (52171090), the National Key Research and Development Program of Ningbo (2024Z154), and the Natural Science Foundation of Ningbo (2023QL050).

Data availability

Data will be made available on request.

References

- C. Dellacorte, Oil-Free shaft support system rotordynamics: past, present and future challenges and opportunities, Mech. Syst. Signal Process. 29 (2012) 67–76.
- [2] C. Dellacorte, K.C. Radil, R.J. Bruckner, Design, fabrication, and performance of open source generation I and II compliant hydrodynamic gas foil bearings, Tribol. Trans. 51 (2008) 254–264.
- [3] H. Heshmat, Operation of foil bearings beyond the bending critical mode, J. Tribol. 122 (2000) 192–198.
- [4] D. Wang, D.S. Su, R. Schlögl, Electron beam induced transformation of MoO_3 to MoO_2 and a new phase MoO, Z. Anorg. Allg. Chem. 630 (2004) 1007–1014.
- [5] S. Veprek, M.G.J. Veprek-Heijman, P. Karvankova, Different approaches to superhard coatings and nanocomposites, Thin Solid Films 476 (2005) 1–29.
- [6] M.E. Cura, X.W. Liu, U. Kanerva, Friction behavior of alumina / molybdenum composites and formation of MoO_{3-x} phase at 400 °C, Tribol. Int. 87 (2015) 23–31.
- [7] G. Gassner, P.H. Mayrhofer, K. Kutschej, Magnéli phase formation of PVD Mo-N and W-N coatings, Surf. Coat. Technol. 201 (2006) 3335–3341.
- [8] Y.P. Zhang, Z.Y. Wang, S.H. Zhou, Synergistic effect of V and Ag diffusion favored the temperature-adaptive tribological behavior of VAIN/Ag multi-layer coating, Tribol. Int. 192 (2024) 109285.
- [9] Z.D. Wang, S.H. Zhou, G.S. Ma, Achieving ultrastrong-tough CrAIN coatings with low friction coefficient by Y incorporating, Ceram. Int. 50 (2024) 23621–23633.
- [10] G.S. Wu, F.L. Song, Y.B. Shi, Effect of multi-doping on the tribological behavior MoN (Ag)-based films in a wide temperature range, J. Mater. Sci. 58 (2023) 3960–3971.
- [11] B. Pavel, J. Peter, M. HUDÁKOVÁ, K. Matej, B. JANA, Cr₂N-7Ag nanocomposite thin films deposited on Vanadis 6 tool steel[J], Appl. Surf. Sci. 307 (2014) 13–19.
- [12] D.V. Shtansky, A.V. Bondarev, V. Kiryukhantsev-Korneevp, Structure and tribological properties of MoCN-Ag coatings in the temperature range of 25-700 °C [J], Appl. Surf. Sci. 273 (2013) 408–414.
- [13] S.M. Aouadi, Y. Paudel, W.J. Simonson, Tribological investigation of adaptive Mo₂N/MoS₂/Ag coatings with highsulfur content, Surf. Coat. Technol. 203 (2009) 1304–1309.
- [14] E. Liu, J. Zhang, S. Chen, High temperature negative wear behaviour of VN/Ag composites induced by expansive oxidation reaction, Ceram. Int. 47 (2021) 15901–15909.

- [15] X. Xu, J. Sun, F. Su, Microstructure and tribological performance of adaptive MoN-Ag nanocomposite coatings with various Ag contents, Wear (2022) 488–489.
- [16] Q.G. Zhang, Y. Zhou, G.J. Zhang, Nanocomposite Mo-Ag-N lubricating, wear resistant and hard coatings fabricated by magnetron sputtering, Mater. Sci. Eng. B 286 (2022) 116066.
- [17] H. Ju, J. Xu, Microstructure. Oxidation resistance, mechanical and tribological properties of Ti-Y-N films by reactive magnetron sputtering, Surf. Coat. Technol. 283 (2015) 311–317.
- [18] Z.Y. Yin, S. Wu, Y.F. Zhang, A comparative study on the structure and properties of TiAlSiN coatings deposited by FCVA and HiPIMS, J. Alloys Compd. 1005 (2024) 175844.
- [19] P.Y. Ying, H.Y. Sun, P. Zhang, Preparation and tribological properties of WS₂ solid lubricating coating with dense structure using HiPIMS, J Mater Res Techno 32 (2024) 530–540.
- [20] M.R. Alhafian, J.B. Chemin, Y. Fleming, Comparison on the structural, mechanical and tribological properties of TiAIN coatings deposited by HiPIMS and Cathodic Arc Evaporation, Surf. Coat. Technol. 423 (2021) 127529.
- [21] J. Ceng, W. Cai, Effect of scratching frequency on the tribocorrosion resistance of Al-Mn amorphous thin films, Wear 426-427 (2019) 1457–1465.
- [22] Q. Cai, S. Li, J. Pu, Effect of multicomponent doping on the structure and tribological properties of VN-based coatings, J. Alloys Compd. 806 (2019) 566–574.
- [23] A.G.C.M. Janssen, M.M. Abdalla, V.F. Keulfn, Celebrating the 100th anniversary of the Stoney equation for film stress: developments from polycrystalline steel strips to single crystal silicon wafers, Thin Solid Films 517 (2009) 1858–1867.
- [24] D. Perea, G. Bejarano, Development and characterization of TiAlN (Ag, Cu) nanocomposite coatings deposited by DC magnetron sputtering for tribological applications, Surf. Coat. Technol. 381 (2020) 125095.
- [25] Z.Y. Wang, X.W. Li, X. Wang, Hard yet tough V-Al-C-N nanocomposite coatings: Microstructure, mechanical and tribological properties, Surf. Coat. Technol. 304 (2016) 553–559.
- [26] A.P. Hu, D.J. Kong, W. Zhu, Effects of residual stresses of TiN coating on its interracial bonding strength, Tool Engineering 3 (2009) 34–36.
- [27] B. Luster, D. Stone, P. Singhd, Textured VN coatings with Ag₃VO₄ solid lubricant reservoirs, Surf. Coat. Technol. 206 (2011) 1932–1935.
- [28] Y.H. Jiang, X.M. Wu, S.N. Bian, Insight into the tribological performance and mechanisms of MoN-Ag/oil solid-liquid lubrication system based on catalytic effect, Surf. Coat. Technol. 480 (2024) 130612.
- [29] W. Gulbiński, T. Suszko, Thin films of Mo₂N/Ag nanocomposite—the structure, mechanical and tribological properties, Surf. Coat. Technol. 201 (2006) 1469–1476.
- [30] M. Fenker, M. Balzer, S. Kellner, Formation of solid lubricants during high temperature tribology of silver-doped molybdenum nitride coatings deposited by dcMS and HIPIMS, Coatings 11 (2021) 1415.
- [31] Y.H. Jiang, X.M. Wu, L.H. Yu, In-situ tribo-induced formation of superb lubricious carbon-based tribofflms on the catalytical active MoN-Ag fflm surfaces, Tribol. Int. 196 (2024) 109715.
- [32] D. Stone, J. Liu, D.P. Singh, Layered atomic structures of double oxides for low shear strength at high temperatures, Scr. Mater. 62 (2010) 735–738.
- [33] C. Muratore, J.E. Bultman, S.M. Aouadi, In situ Raman spectroscopy for examination of high temperature tribological processes, Wear 270 (2011) 140–145.
- [34] X. Xu, F. Su, Z. Li, Microstructure and tribological behaviors of MoN-Cu nanocomposite coatings sliding against Si₃N₄ ball under dry and oil-lubricated conditions, Wear 434 (2019) 202994.
- [35] S.F. Zaman, N. Pasupulety, A.A. Al-Zahrani, Carbon monoxide hydrogenation on potassium promoted Mo₂N catalysts, Appl. Catal. A. Gen. 532 (2016) 133–145.
- [36] X. Xu, J.F. Sun, F.H. Su, Microstructure and tribological performance of adaptive MoN-Ag nanocomposite coatings with various Ag contents, Wear 488–489 (2021) 204170.
- [37] T.T. Zhang, C.B. Huang, H. Lan, et al., Tribological properties and lubrication mechanisms of a Ag-Mo composite[J], Lubr. Sci. 28 (2016) 141–156.
- [38] E. Wenda, High temperature reactions in the MoO₃-Ag₂O system, J. Therm. Anal. 53 (1998) 861–870.
- [39] J.H. Hsieh, C.H. Chiu, C. Li, Development of anti-wear and anti-bacteria TaN-(Ag, Cu) thin films-a review[J], Surf. Coat. Technol. 233 (2013) 159–168.
- [40] C.P. Mulligan, T.A. Blanchet, D. Gall, CrN-Ag nanocomposite coatings: High-temperature tribological response, Wear 269 (2010) 125–131.
- [41] B. Pavel, J. Peter, HudákováM, Cr₂N-7Ag nanocomposite thin films deposited on Vanadis 6 tool steel, Appl. Surf. Sci. 307 (2014) 13–19.
- [42] C.P. Mulligan, P.A. Papi, D. Gall, Ag transport in CrN-Ag nanocomposite coatings, Thin Solid Films 520 (2012) 6774–6779.
- [43] J. Hu, C. Muratore, A. Voevodin, Silver Diffusion and High-Temperature Lubrication Mechanisms of YSZ-Ag-Mo based Nanocomposite Coatings, Compos. Sci. Technol. 67 (2007) 336–347.
- [44] W. Gulbinski, T. Suszko, Thin films of MoO₃-Ag₂O binary oxides—the high temperature lubricants, Wear 261 (2006) 867–873.
- [45] S.M. Aouadi, Y. Paudel, B. Luster, Adaptive Mo₂N/MoS₂/Ag tribological nanocomposite coatings for aerospace applications, Tribol. Lett. 29 (2008) 95–103.